

# Synthesis, Morphological, and Electro-optical Characterizations of Metal/Semiconductor Nanowire Heterostructures

Markus Glaser,<sup>†</sup> Andreas Kitzler,<sup>†</sup> Andreas Johannes,<sup>‡</sup> Slawomir Prucnal,<sup>§</sup> Heidi Potts,<sup>||</sup> Sonia Conesa-Boj,<sup>||</sup> Lidija Filipovic,<sup>⊥</sup> Hans Kosina,<sup>⊥</sup> Wolfgang Skorupa,<sup>§</sup> Emmerich Bertagnolli,<sup>†</sup> Carsten Ronning,<sup>‡</sup> Anna Fontcuberta i Morral,<sup>||</sup> and Alois Lugstein<sup>\*,†</sup>

<sup>†</sup>Institute of Solid State Electronics, TU Wien, Floragasse 7, 1040 Wien, Austria

<sup>‡</sup>Institute for Solid State Physics, Friedrich-Schiller-University Jena, Max-Wien-Platz 1, 07743 Jena, Germany

<sup>§</sup>Institute of Ion Beam Physics and Materials Research, Helmholtz-Zentrum Dresden-Rossendorf, Bautzner Landstraße 400, 01328 Dresden, Germany

<sup>||</sup>Laboratoire des Matériaux Semiconducteurs, Ecole Polytechnique Fédérale de Lausanne, 1015 Lausanne, Switzerland

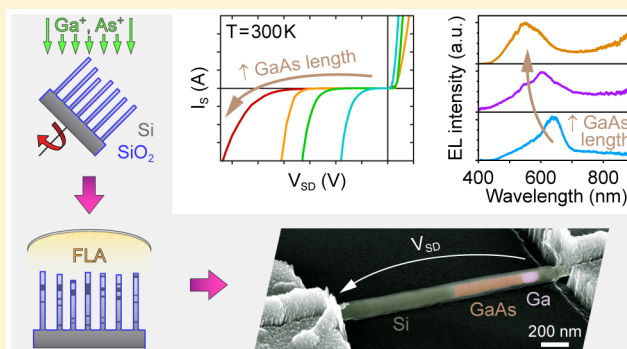
<sup>⊥</sup>Institute for Microelectronics, TU Wien, Gußhausstraße 25-29, 1040 Wien, Austria

## Supporting Information

**ABSTRACT:** In this letter, we demonstrate the formation of unique Ga/GaAs/Si nanowire heterostructures, which were successfully implemented in nanoscale light-emitting devices with visible room temperature electroluminescence. Based on our recent approach for the integration of InAs/Si heterostructures into Si nanowires by ion implantation and flash lamp annealing, we developed a routine that has proven to be suitable for the monolithic integration of GaAs nanocrystallite segments into the core of silicon nanowires. The formation of a Ga segment adjacent to longer GaAs nanocrystallites resulted in Schottky-diode-like  $I/V$  characteristics with distinct electroluminescence originating from the GaAs nanocrystallite for the nanowire device operated in the reverse breakdown regime.

The observed electroluminescence was ascribed to radiative band-to-band recombinations resulting in distinct emission peaks and a low contribution due to intraband transition, which were also observed under forward bias. Simulations of the obtained nanowire heterostructure confirmed the proposed impact ionization process responsible for hot carrier luminescence. This approach may enable a new route for on-chip photonic devices used for light emission or detection purposes.

**KEYWORDS:** Nanowires, heterostructures, Schottky, GaAs, Si, electroluminescence



A successful implementation of a new class of materials or means of processing has a potential impact on long-term future technology nodes. Fundamental investigations of electronic and optical properties of nanowire (NW) heterostructures thus triggered tremendous research on novel device concepts.<sup>1–3</sup> Particularly, integrating photonic devices into the Si platform is a challenge that requires the development of elaborate device designs.<sup>4</sup> Nanoscale Si-based photonic devices would provide full compatibility with mature IC manufacturing processes; yet owing to the inherent disadvantages of the indirect Si band gap, no efficient light emission can be obtained. A hybrid Si platform, integrating III–V functionality into Si nanostructures, would give access to a wide range of high-speed electronic and high-performance photonic applications. However, the diverse natures of the III–V and Si device approaches, material technologies, and processing have posed a significant obstacle in the route for Si-based hybrid optoelectronic systems in the past. Within the last years, a few approaches for Si-based hybrid NW formation via bottom-up growth techniques<sup>5,6</sup> or in

combination with substrate etching<sup>7</sup> were presented, which are restricted to semiconductors, with limitations in epitaxial integration and in retaining the NW morphology. Recently, we published a novel approach for integrating III–V nanocrystallites (NCs) into Si NWs by combining ion implantation and flash lamp annealing, yielding InAs/Si NW heterostructures.<sup>8</sup> Within this study we present this approach to be capable for integrating GaAs NCs into crystalline Si NWs. Due to a modification of the ion implantation routine, NCs with increased axial lengths are obtained, exhibiting a metallic Ga segment adjacent to the GaAs NCs. Such wired NC configuration ensures directed current flow through the abrupt heterointerfaces.

**Received:** January 25, 2016

**Revised:** April 13, 2016

**Published:** May 11, 2016

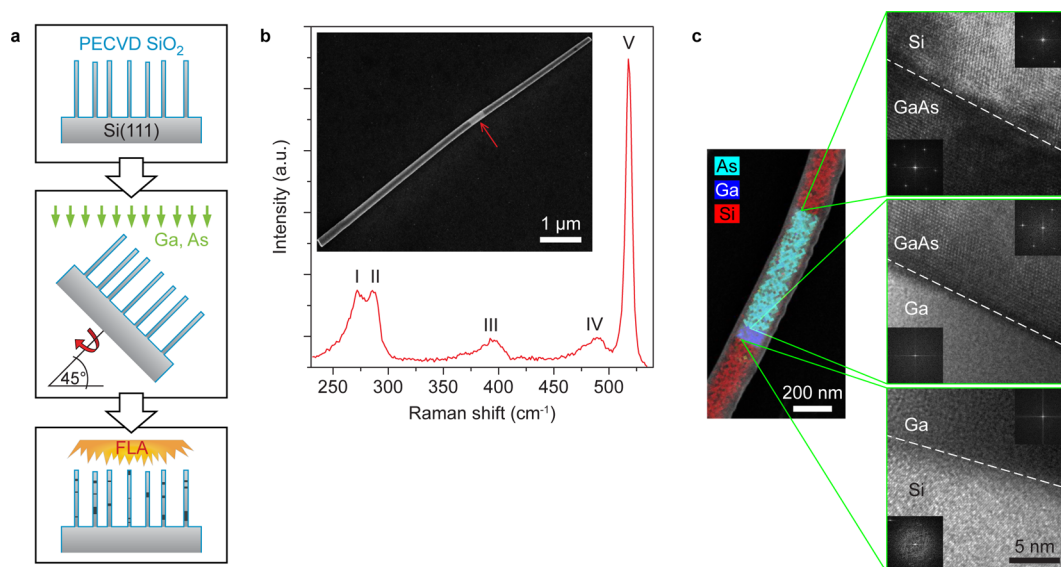


**Figure 1.** Processing and material characterization of Ga/GaAs/Si NW heterostructures. (a) Processing scheme: epitaxial VLS-grown Si  $\langle 111 \rangle$  NWs covered with 20 nm  $\text{SiO}_2$ ; room temperature ion implantation of Ga and As (2 at% each) with samples mounted on a  $45^\circ$  tilted and rotating specimen holder; formation of wired GaAs NCs after 20 ms FLA ( $54.2 \text{ J/cm}^2$ ). (b) SEM image of a single Ga/GaAs/Si NW heterostructure with the respective  $\mu$ -Raman spectrum acquired from the center of the GaAs NC (red arrow). Denoted peaks are identified as (I) GaAs TO,  $272 \text{ cm}^{-1}$ ; (II) GaAs surface phonon,  $287 \text{ cm}^{-1}$ ; (III) local vibrational modes of Si-doped GaAs,  $360\text{--}410 \text{ cm}^{-1}$ ; (IV) nanocrystalline Si,  $487.5 \text{ cm}^{-1}$ ; and (V) Si zone center phonon mode,  $517.9 \text{ cm}^{-1}$  (see Supporting Information 3 for details). (c) SEM image of a Ga/GaAs/Si NW heterostructure with  $\text{SiO}_2$  shell and Si, Ga, and As maps acquired from TEM-EDX analysis shown as a color overlay. HRTEM detail micrographs of the axial interfaces are shown in the right panel along with the respective fast Fourier transforms of the crystalline zinc-blende Si and GaAs and amorphous Ga segments in the insets.

We achieved the monolithic integration of GaAs and Ga/GaAs NCs into Si NWs by exploring ion implantation and flash lamp annealing (FLA) routines. Such application of mature semiconductor processing techniques<sup>9</sup> allows to process wafer-scale NW samples along with excellent control of NW morphologies. The main processing steps for NW heterostructure formation are sketched in Figure 1a.

The samples consisted of  $\langle 111 \rangle$  oriented zinc-blende Si NWs epitaxially grown on Si(111) substrates via the gold-catalyzed vapor–liquid–solid (VLS) approach.<sup>10</sup> A low pressure chemical vapor deposition system was utilized for NW growth, using  $\text{SiH}_4$  (2% diluted in He) as precursor gas, a growth temperature of  $T = 788 \text{ K}$  and a total pressure of  $p = 4 \text{ mbar}$ , which resulted in epitaxial and single crystalline NWs with typical lengths of  $10 \mu\text{m}$  and mean diameters of about  $130 \text{ nm}$ . Prior to high fluence implantation of Ga and As ions, the gold catalyst was removed, and a 20 nm thick  $\text{SiO}_2$  layer had to be deposited by plasma enhanced chemical vapor deposition, acting as a protective mold during implantation and millisecond FLA. In order to achieve a homogeneous ion distribution and to avoid bending of the NWs due to high fluence ion bombardment,<sup>11</sup> samples were mounted on a  $45^\circ$  tilted stage and continuously rotated during ion implantation. Due to nanostructure-related peculiarities of ion beam induced sputtering, implantation parameters were derived from 3D Monte Carlo simulations using *iradina*.<sup>12</sup> Ga and As ions were implanted alternately, resulting in a nominal concentration of 2 at % Ga and 2 at % As inside the NW core. Full amorphization and a significant shortening as well as a change of the NW cross-section from hexagonal to circular was observed due to plastic deformation of NWs during ion implantation.<sup>13</sup> Remarkably, the  $\text{SiO}_2$  shell was found to persist during implantation with little intermixing at the interface to the Si core (see Supporting Information 1). Finally the phase separation and actual formation of NW

heterostructures by liquid phase epitaxy (LPE)<sup>14</sup> was induced by a 3 min preheating at  $600^\circ\text{C}$  and subsequent 20 ms FLA, whereby the  $\text{SiO}_2$  shell stabilized the molten core of the NWs. FLA was performed in Ar atmosphere with a flash energy of  $54.2 \text{ J/cm}^2$ , resulting in peak sample temperatures of approximately  $1470 \text{ K}$ .<sup>8</sup> Within the cooling period after FLA, GaAs NCs formed with lengths varying from approximately  $10 \text{ nm}$  to  $1 \mu\text{m}$  (cf. Supporting Information 2). In addition, an adjacent Ga segment was observed for NCs exceeding a length of about  $75 \text{ nm}$ .

The composition, morphology, and crystallinity of such obtained NW heterostructures were analyzed in detail by  $\mu$ -Raman spectroscopy, transmission electron microscopy (TEM), and energy dispersive X-ray spectroscopy (EDX). Figure 1b shows a typical  $\mu$ -Raman spectrum acquired from the GaAs NC depicted in the scanning electron microscopy (SEM) image. The main Raman features were identified as the transverse optical (TO) phonon mode of crystalline GaAs (peak I), a GaAs related surface phonon mode due to the cylindrical shape of the GaAs NC (peak II),<sup>15</sup> and GaAs local vibrational modes (peak III).<sup>16</sup> The occurrence of GaAs local vibrational modes indicates a high concentration of Si atoms occupying Ga or As lattice sites. As the excitation laser spot exceeds the GaAs NC size, Raman features arising from the adjacent Si NW (peak IV, V) were also detected (see Supporting Information 3).

Extensive high resolution TEM (HRTEM) and EDX analysis confirmed composition and crystallinity of both the Si and GaAs segments with abrupt interfaces as indicated by Raman investigations (see Supporting Information 4). Although a rapid annealing step was applied, consisting of melting of the NW core during the 20 ms FLA step and recrystallization during subsequent cooling, only a low number of crystallographic defects of the NW heterostructure were observed in TEM

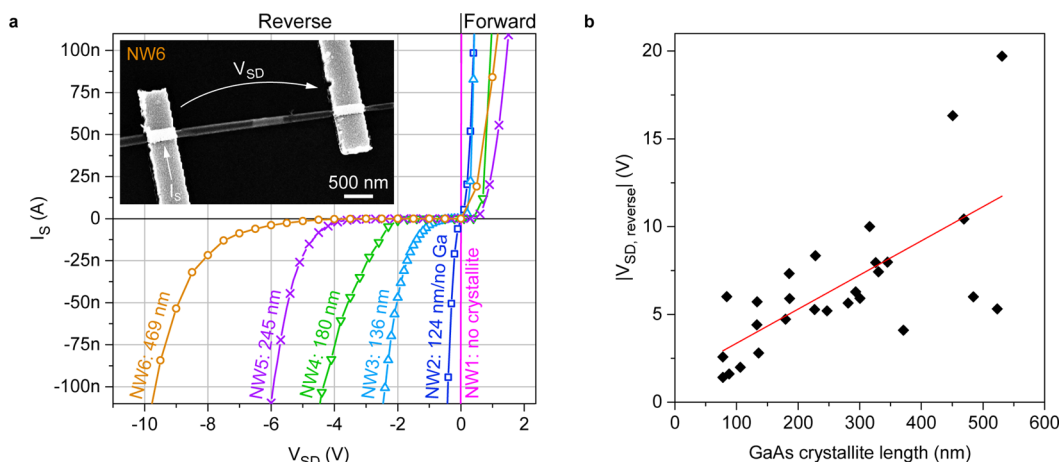


**Figure 2.** Electrical characterization of selected NW heterostructures. (a)  $I/V$  characteristics of a processed Si NW without NCs (NW1), a Si NW heterostructure with a GaAs NC (NW2), and four Si NWs with Ga/GaAs NCs (NW3–NW6). Axial lengths of the GaAs NCs are for NW2:124 nm ( $\square$ ), NW3:136 nm ( $\triangle$ ), NW4:180 nm ( $\nabla$ ), NW5:245 nm ( $\times$ ), and NW6:469 nm ( $\circ$ ). The inset shows the SEM image of NW6 with electrical contacts, and the direction of the bias  $V_{SD}$  applied to the source contact next to the Ga segment is depicted. The drain contact and the Si substrate are grounded. (b) Scatter diagram of  $|V_{SD, reverse}|$  values of measured NW heterostructures under reverse bias at  $|I_S| = 200$  nA as a function of GaAs NC length with a linear fitting curve.

investigations (see [Supporting Information 5](#)). As mentioned above, for larger GaAs NCs, we observed the formation of amorphous Ga segments, separating the GaAs NCs from the Si NW core. Previous investigations indicated a liquid state for nanoscale Ga droplets at room temperature,<sup>17</sup> which may also apply for the observed amorphous structure of the Ga segments. Further EDX revealed As within the recrystallized Si NWs, thus expecting n-type doping of the Si NW. In the HRTEM images of [Figure 1c](#), the respective interfaces of the axially aligned Si/Ga/GaAs/Si segments are shown. Remarkably, the Si NWs, although fully amorphous after ion implantation, recrystallize in  $\langle 111 \rangle$  directions along the NW axis during LPE, which is also the predominant growth direction for VLS-grown Si NWs with diameters above 40 nm.<sup>18</sup> The embedded zinc-blende GaAs NCs adopt the crystallite direction of the Si NW as shown in the fast Fourier transform patterns in [Figure 1c](#). Furthermore, the amorphous Ga segment formed next to larger GaAs NCs exhibits an abrupt interface to both the GaAs and the Si NWs.

To determine the electrical transport properties of wired GaAs NCs embedded in Si NWs, individual NW heterostructures were integrated in four-terminal and two-terminal (cf. inset in [Figure 2a](#)) devices resembling a back-gated NW field effect transistor with a 120 nm thick  $\text{SiO}_2$  layer as gate dielectric and the substrate as common gate. Electrical contacts to nanowire devices were processed by e-beam lithography, e-beam evaporation of Ni, and lift off techniques.

The  $I/V$  characteristics of a contacted Si NW without a NC exhibits linear behavior (NW1 in [Figure 2a](#)) and four-terminal measurements revealed a resistivity of  $1.1 \text{ m}\Omega\text{-cm}$ . Unambiguously n-type doping was confirmed by thermoelectric measurements on individually contacted Si NWs (see [Supporting Information 6](#)). Assuming As as the dopant, this corresponds to a bulk impurity concentration of approximately  $8.6 \times 10^{19} \text{ cm}^{-3}$  and thus degenerate doping of the Si NWs.<sup>19</sup> Due to the high doping of the Si NW and the present  $\text{SiO}_2$  shell, influences of surface states or adsorbates on the electronic structure of the NW core were assumed to be negligible. Furthermore, the low resistivity of the Si NWs impeded the use

of capacity-dependent scanning probe microscopy to investigate NW doping.

For the NWs with GaAs NCs and Ga/GaAs hybrids, no such direct experimental determination of the doping type could be achieved. However, as GaAs grown from a Si-rich high temperature melt by LPE results in n-type GaAs crystals,<sup>20</sup> n-type doping was also assumed to be prevailing in the present GaAs NCs. Furthermore, rectifying Ga/GaAs contacts only form with n-type GaAs,<sup>21</sup> which agrees well with the Schottky-type behavior of the Ga/GaAs heterostructures (NW3–NW6 in [Figure 2a](#)). The resistivity of the GaAs NCs was measured to be approximately  $6 \text{ }\Omega\text{-cm}$ , which corresponds to an effective impurity concentration of  $1.5 \times 10^{14} \text{ cm}^{-3}$  in n-type GaAs.<sup>19</sup> However, Raman investigations (cf. [Supporting Information 3](#)) indicate considerably higher Si impurity concentrations of about  $5 \times 10^{18} \text{ cm}^{-3}$ .<sup>22</sup> Thus, we can conclude that, due to the amphoteric nature of Si dopants in GaAs, compensation doping results in overall moderately doped n-type GaAs NCs.

The highly n-type doped Si NWs aligned with a 124 nm long GaAs NC (NW2 in [Figure 2a](#)) results in a quantum-barrier-like structure with a barrier height for conduction electrons of about 67.8 meV (see simulation results in [Supporting Information 7](#)). In contrast to the n-type Si NWs for which ohmic behavior was observed (cf. NW1), a strongly nonlinear but symmetric behavior is observed, which is typical for field-induced tunneling currents that increase steeply when the effective tunneling barrier narrows for ascending bias voltages. Temperature-dependent  $I/V$  measurements, at a small bias voltage of 10 mV to minimize band-bending and tunneling effects, yielded an effective barrier height of approximately 50 meV, which is in reasonable agreement with semiclassical device simulations (see [Supporting Information 7](#)).

For NW heterostructures with a Ga segment adjacent to the GaAs NC, the Ga/GaAs Schottky junction dominates the  $I/V$  characteristics, resulting in a distinct rectifying behavior (NW3–NW6 in [Figure 2a](#)).  $I/V$  characteristics are further labeled forward (reverse) for positive (negative) bias  $V_{SD}$  applied to the NW end facing the Ga segment. According to the simulated energy band diagram under forward bias (right panel in [Figure 3](#)) conduction electrons encounter the small



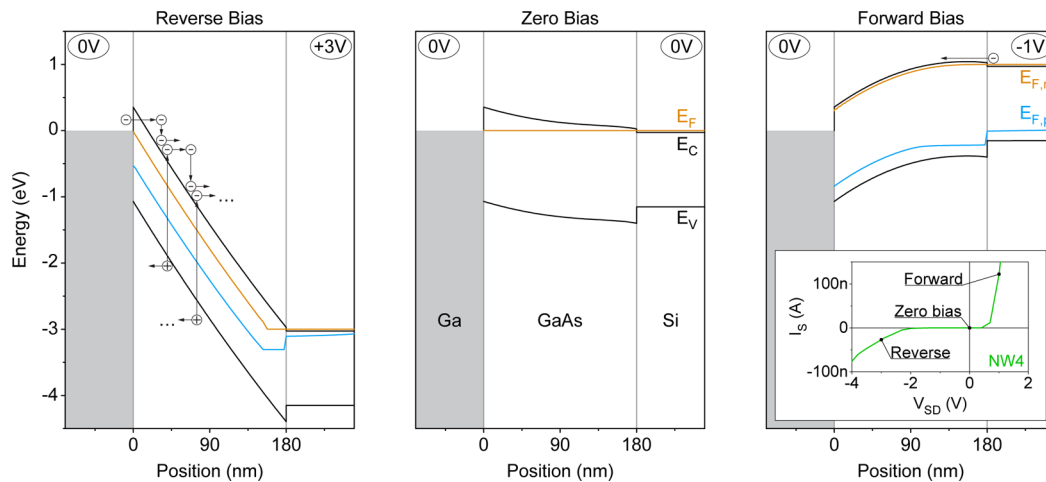


**Figure 3.** Simulated energy band diagrams. Band diagrams of a Ga/GaAs/Si heterostructure similar to NW4, calculated with the semiclassical device simulator Minimos-NT under reverse (left panel), zero (center panel), and forward (right panel) bias conditions.  $E_V$  denotes the valence band maximum and  $E_C$  the conduction band minimum. The Fermi level as well as the electron and hole quasi Fermi levels are denoted by  $E_F$ ,  $E_{F,n}$ , and  $E_{F,p}$ , respectively. The heterojunctions were assumed to be defect-free, and the work function of Ga was fixed to 4.3 eV.<sup>23</sup> Under nonzero bias conditions, the main drift component of the current is sketched as electrons ( $\ominus$ ) entering the GaAs NC by tunneling through the Ga/GaAs Schottky junction (reverse bias) or the Si/GaAs heterojunction (forward bias). The cascade process responsible for generating electron–hole ( $\oplus$ ) pairs due to impact ionization of hot charge carriers is shown for the device operated under reverse bias. The inset shows the  $I/V$  characteristics of NW4 with marked operating points for the three bias conditions.

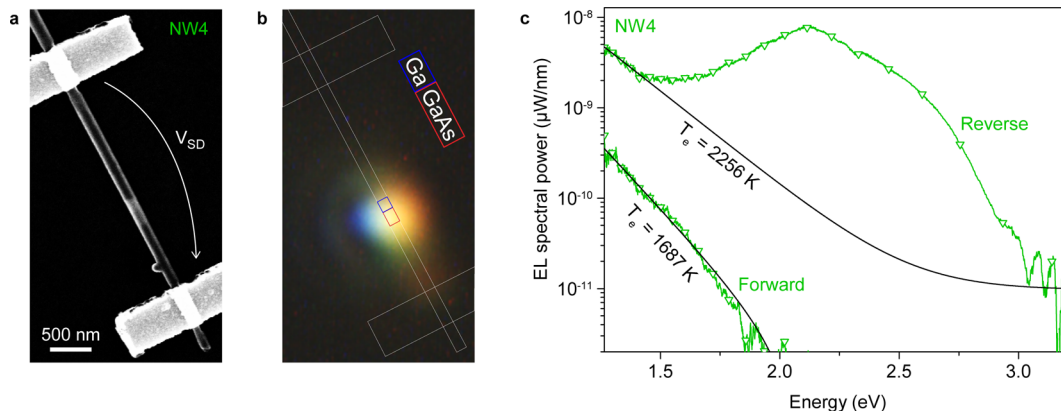


**Figure 4.** Room temperature EL of a Ga/GaAs/Si NW heterostructure device. (a) SEM image, showing the two-terminal device (NW4) with a Ga segment next to a 180 nm long GaAs NC. (b) Optical microscope image (1 min exposure time) of the same device under reverse bias conditions ( $V_{SD} = -9.4$  V,  $I_s = -4$   $\mu$ A) with visible EL originating from the GaAs NC. Spectral decomposition of the EL spot is due to artifacts of the imaging system. (c) Corrected EL spectra acquired from NW4 under forward bias ( $V_{SD} = 4.85$  V,  $I_s = 8.3$   $\mu$ A) and reverse bias ( $V_{SD} = -9.4$  V,  $I_s = -4$   $\mu$ A). Black curves are fittings according to eq 1, representing luminescence ascribed to Bremsstrahlung. Under reverse bias, band-to-band EL is superimposed, whereas under forward bias only Bremsstrahlung can be seen at high field conditions.

barrier at the Si/GaAs interface with a turn on voltage of around 0.2–0.6 V.

For such Si NW heterostructures containing a Ga/GaAs segment, Schottky barrier heights in the range of 186–330 meV were obtained from temperature-dependent  $I/V$  measurements. With  $e$  the elementary charge,  $\chi = 4.07$  eV the electron affinity and  $e\phi_m = 4.3$  eV the work function of GaAs,<sup>23</sup> the Schottky barrier height of an ideal Ga/GaAs junction can be calculated to  $e\phi = e\phi_m - \chi \approx 230$  meV. In literature, Schottky barrier heights of Ga/n-GaAs junctions are usually larger than 1 eV, owing to Fermi level pinning caused by defects at the interface.<sup>21</sup> Thus, a reasonable low number of interface defects due to the absence of Fermi level pinning can be assumed for the obtained Ga/GaAs Schottky junctions within NW heterostructures.

Under reverse bias conditions, the voltage is supported across the drift region of the Schottky contact with the

maximum electric field located at the Ga/GaAs interface. Due to a weak barrier lowering, the leakage current rises gradually with reverse bias as thermally excited electrons in the metal surmount the barrier. However, as the field increases further, a fraction of high energy carriers fail to lose energy by phonon emission, attaining energies in excess of the material bandgap and lose energy by creating electron–hole pairs, a process generally known as impact ionization.<sup>24,25</sup> At a crucial breakdown field, these generated carriers gain sufficient energies to induce further impact ionizations cascades leading to avalanche carrier multiplication (left panel in Figure 3).

Simulations of the reverse biased NW heterostructure yielded high impact ionization rates in the GaAs NC next to the Schottky interface, proportional to the applied bias (see Supporting Information 8). Since negligible voltage is supported within the metal and the degenerately doped Si

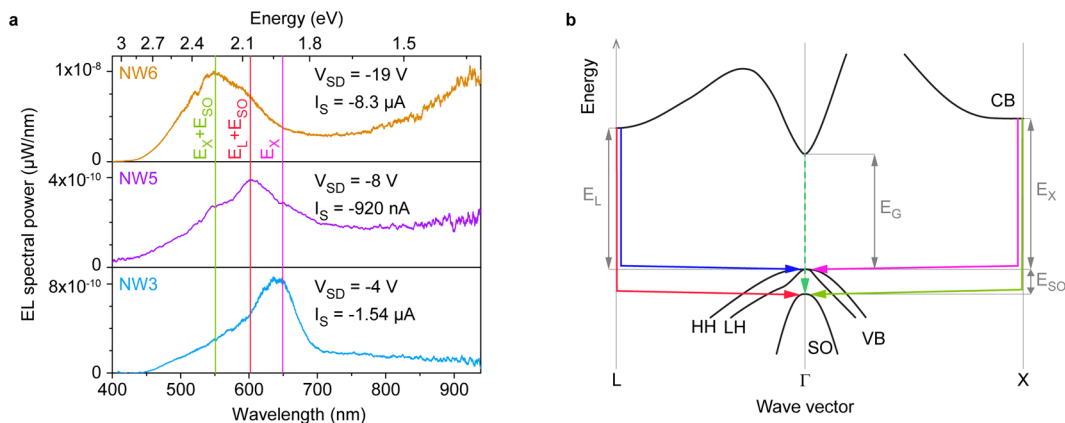


**Figure 5.** EL spectra with designated transition energies. (a) Room temperature EL spectra obtained from NW3, NW5, and NW6 and the respective bias parameters. Vertical lines denote transition energies for the radiative b–b recombinations correlating with maxima in the presented EL spectra. (b) Sketch of the GaAs energy band structure between the Brillouin zone symmetry points L,  $\Gamma$ , and X with the lowest conduction band, heavy-hole, light-hole, and split-off valence bands with the relevant energies obtained from ref 28:  $E_G = 1.42$  eV,  $E_L = 1.72$  eV,  $E_X = 1.91$  eV, and  $E_{SO} = 0.34$  eV. Radiative b–b recombinations identified by energy values of maxima in EL spectra of investigated NW devices are shown with colored arrows. Solid and dashed lines denote indirect (phonon-assisted) and direct transitions, respectively.

NW, the reverse blocking capability of the Schottky rectifier is governed by the GaAs NC, and the breakdown voltage thereby appears to be linearly dependent on the length of the NC, as shown in Figure 2b.

Operating the Ga/GaAs/Si NW heterostructure devices under reverse bias in the avalanche breakdown regime resulted in broadband light emission, clearly originating from the GaAs NCs. In Figure 4 an SEM image of the two-terminal device (Figure 4a) and an optical microscope image (Figure 4b) are shown, demonstrating distinct electroluminescence (EL) of NW4 under reverse bias conditions. The associated EL spectrum for the device operated under reverse and forward bias conditions is depicted in Figure 4c. The measured EL spectra were corrected according to transmission data obtained from calibrating the spectroscopy equipment with a calibrated halogen light source.

Pronounced features were observed in the EL spectra above the GaAs band gap energy  $E_G = 1.42$  eV, which are assigned to radiative band-to-band (b–b) recombinations. A continuous background in the EL spectrum extending to the near-infrared is ascribed to intraband transitions, or Bremsstrahlung.<sup>26,27</sup>

Under high forward biases, the weak EL appears to be consisting of Bremsstrahlung only. Assuming a Maxwellian distribution for electrons and a bulk density of states with simple parabolic energy bands, the rate  $R$  for light emission ascribed to Bremsstrahlung at an energy  $E$  is proportional to<sup>27</sup>

$$R \propto \sqrt{E} \exp\left(-\frac{E}{k_B T_e}\right) \quad (1)$$

with  $k_B$  the Boltzmann constant and  $T_e$  the electron temperature. Values for  $T_e$ , obtained by fitting eq 1 to EL spectra, assuming the electron energy distribution to be reproduced by the photon energy distribution, are in good agreement with temperatures of hot electrons in GaAs high-electron-mobility transistors.<sup>26</sup>

In general, considerably higher EL intensities were observed under reverse bias conditions. Bremsstrahlung corresponding to  $T_e = 2256$  K and superimposed b–b recombinations constitute the EL spectra, as shown in Figure 4c for such a reverse biased device. For a more detailed analysis of the b–b recombination related EL, Ga/GaAs/Si NW heterostructures with increasing

GaAs NC lengths and thus increasing breakdown voltages were investigated. Figure 5a shows EL spectra of three NW heterostructures, exemplarily selected out of 30 investigated devices, which all exhibited similar EL characteristics.

Operated under reverse bias conditions (cf. Figure 2a), these devices exhibited a broad visible EL extending to the near-infrared. Notably, there is no distinct emission peak that may be assigned to the band gap energy  $E_G = 1.42$  eV of GaAs (cf. Figure 5b). Under reverse bias, the voltage is supported across the drift region of the Schottky contact. As the moderately doped GaAs NC is embedded between a metallic and a degenerately doped (i.e., highly conducting) Si NW, the maximum electric field, exceeding  $2 \times 10^5$  V/cm, is supposed to be located in the GaAs NC. At such high electric fields, the conduction band  $\Gamma$  valley population is approaching zero with high populations of the X and L valleys,<sup>25</sup> diminishing direct  $\Gamma$  valley transitions (i.e., EL at the GaAs band gap energy).

For EL in the visible spectral range, distinct emission peaks can be observed with the overall maximum shifting to higher energies for longer GaAs NCs, i.e., increasing breakdown voltages (cf. Figure 2b). These distinct EL peaks are assigned to hot carrier luminescence<sup>26,27,29</sup> with the respective phonon-assisted radiative b–b recombinations as sketched in the GaAs energy band structure in Figure 5b. Due to the necessity of energy and momentum conservation, light emission arising from b–b recombinations requires electrons to be scattered from the indirect conduction band valleys to the zone center ( $k \approx 0$ ). High phonon density of states are related to a large number of phonon states for a certain energy in the phonon dispersion, i.e., parts of phonon dispersion curves with almost zero slope.<sup>30</sup> In the case of GaAs, the phonon dispersion of all kinds of involved phonons exhibit approximately zero slope at the X- and L-symmetry points.<sup>31</sup> Thus, a high density of states of phonons with the respective wave vectors are available for scattering electrons to the zone center by emission or absorption of such phonons, resulting in the observed EL maxima. The involvement of split-off band holes in radiative b–b recombinations in GaAs was also observed in photoluminescence studies.<sup>32</sup> However, the respective b–b transitions require adequate electron population of the L and X valley, as well as holes in the heavy-hole, light-hole, and split-off

band.<sup>29</sup> The formation of hot charge carriers in  $\langle 111 \rangle$  oriented GaAs NCs further requires electrons to gain energies higher than the impact ionization threshold (1.8–2 eV)<sup>25,33</sup> through scattering events, changing their  $k$ -vector.<sup>24</sup>

The proposed hot charge carrier generation mechanism is sketched in the left panel of Figure 3 with electrons tunneling from Ga through the Schottky barrier into the GaAs NC. Under reverse bias, a high electric field is present in the GaAs depletion layer adjacent to the Schottky interface, accelerating charge carriers, which in turn attain energies in excess of the impact ionization threshold. Such hot carriers, instead of transferring energy to phonons, lose energy by elevating valence band electrons to the conduction band and these generated electron–hole pairs themselves generate carrier pairs and the process enters runaway. Simulations of the actual structures confirmed impact ionization and also high yields of holes adjacent to the Ga/GaAs Schottky junction (see Supporting Information 8). Remarkably, with increasing bias voltages, EL emission extends further into the GaAs NC, which is consistent with the impact ionization generation rate simulations.

Radiative recombinations and intraband electron scattering thus result in the characteristic EL spectra with contributions from b–b recombinations and Bremsstrahlung. This confirms the assumed avalanche process with hot electrons injected from Ga into the GaAs NC, generating holes and resulting in the observed EL. Such single-nanowire light emitters yielded external quantum efficiencies of up to  $\text{EQE} = \int (P_{\text{sp}}/E_{\lambda})(e/I) d\lambda = 8.9 \times 10^{-7}$ , where the emitted spectral power  $P_{\text{sp}}$  was obtained from integrating the EL spectral power in the wavelength range  $\lambda = 400$ –1000 nm.  $E_{\lambda}$  is the energy of a photon with wavelength  $\lambda$ ,  $I$  the applied NW current, and  $e$  the elementary charge. However, including the numerical aperture of the spectroscopy system and considering a homogeneously light emitting GaAs segment with a cylindrical shape, this results in a high EL spectral power density of 14.8 mW/cm<sup>2</sup>.

In conclusion, we demonstrated effective EL from avalanche light-emitting diodes in self-assembled metal/semiconductor NW heterostructures. The axially aligned Si/Ga/GaAs/Si NW heterostructures were achieved via a novel approach, combining VLS NW growth, ion implantation, and millisecond FLA. The visible spectrum of the EL is dominated by hot carrier luminescence due to impact ionization, revealing distinct maxima, which are correlated with GaAs interband transitions. A low broadband exponential component of the EL is ascribed to Bremsstrahlung. A considerable benefit of the presented approach to process heterostructures within Si NWs is the advantageous condition for combining highly mismatched materials, provided by efficient strain relaxation. Recent experiments already supplied evidence for this method to be applicable to other highly mismatched III–V/Si heterostructures, namely, InAs or InGaAs. Furthermore, this unique method is suitable for integrating axial metal segments into Si NWs, by only implanting metal ions. In this study, single NW heterostructures were investigated to gain insight into the fundamental properties of the processed light emitting devices. However, this method could readily be applied to process a large scale device consisting of straight Si NW arrays on bulk Si, allowing to significantly increase device performances due to parallel operation of numerous NW heterostructures.

## ■ ASSOCIATED CONTENT

### ■ Supporting Information

The Supporting Information is available free of charge on the ACS Publications website at DOI: 10.1021/acs.nanolett.6b00315.

SEM investigations of nanowire response on ion implantation and annealing, thin crystallite formation, detailed Raman and TEM-EDX investigations, experimental determination of Si nanowire doping type, simulations of Si/GaAs/Si barrier heights, hole concentrations, and impact ionization generation rates (PDF)

## ■ AUTHOR INFORMATION

### Corresponding Author

\*E-mail: alois.lugstein@tuwien.ac.at.

### Notes

The authors declare no competing financial interest.

## ■ ACKNOWLEDGMENTS

The authors thank Michael Stöger-Pollach from the USTEM at TU Wien for providing EFTEM analysis of nanowire slices as well as Oskar Baumgartner from Global TCAD Solutions for his support in setting up simulations. We gratefully acknowledge financial support by the Austrian Science Fund (FWF) project No. I 724-N16 and the Deutsche Forschungsgemeinschaft (DFG) project No. R01198/14-1 and thank the Swiss National Science Foundation (SNF) for funding through NCCR-QSIT. We would also like to acknowledge the ITN network “NanoEmbrace”. Furthermore, we thank the interdisciplinary Centre for Electron Microscopy (CIME) at EPFL for access to and training of the electron microscopes. The cleanroom facilities were provided by the Center for Micro- and Nanostructures (ZMNS) at TU Wien.

## ■ ABBREVIATIONS

EDX, energy dispersive X-ray spectroscopy; EL, electroluminescence; FLA, flash lamp annealing; HRTEM, high-resolution transmission electron microscopy; LPE, liquid phase epitaxy; NC, nanocrystallite; NW, nanowire; SEM, scanning transmission electron microscopy; TEM, transmission electron microscopy; VB, valence band; VLS, vapor–liquid–solid

## ■ REFERENCES

- (1) Yan, R.; Gargas, D.; Yang, P. *Nat. Photonics* **2009**, 3 (10), 569–576.
- (2) Wallentin, J.; Anttu, N.; Asoli, D.; Huffman, M.; Åberg, I.; Magnusson, M. H.; Siefer, G.; Fuss-Kailuweit, P.; Dimroth, F.; Witzigmann, B.; Xu, H. Q.; Samuelson, L.; Deppert, K.; Borgström, M. T. *Science* **2013**, 339 (6123), 1057–1060.
- (3) Bryllert, T.; Wernersson, L.-E.; Froberg, L. E.; Samuelson, L. *IEEE Electron Device Lett.* **2006**, 27 (5), 323–325.
- (4) Lockwood, D. J.; Pavesi, L. *Silicon Photonics; Topics in Applied Physics*; Springer: Berlin Heidelberg, 2004; pp 1–50.
- (5) Hocevar, M.; Immink, G.; Verheijen, M.; Akopian, N.; Zwiller, V.; Kouwenhoven, L.; Bakkers, E. *Nat. Commun.* **2012**, 3, 1266.
- (6) Conesa-Boj, S.; Dunand, S.; Russo-Averchi, E.; Heiss, M.; Ruffer, D.; Wyrsh, N.; Ballif, C.; Fontcuberta i Morral, A. *Nanoscale* **2013**, 5 (20), 9633–9639.
- (7) Borg, M.; Schmid, H.; Moselund, K. E.; Signorello, G.; Gignac, L.; Bruley, J.; Breslin, C.; Das Kanungo, P.; Werner, P.; Riel, H. *Nano Lett.* **2014**, 14 (4), 1914–1920.

- (8) Prucnal, S.; Glaser, M.; Lugstein, A.; Bertagnolli, E.; Stöger-Pollach, M.; Zhou, S.; Helm, M.; Reichel, D.; Rebohle, L.; Turek, M.; Zuk, J.; Skorupa, W. *Nano Res.* **2014**, *7* (12), 1769–1776.
- (9) Fiory, A. T. *J. Electron. Mater.* **2002**, *31* (10), 981–987.
- (10) Wang, N.; Cai, Y.; Zhang, R. Q. *Mater. Sci. Eng., R* **2008**, *60* (1–6), 1–51.
- (11) Borschel, C.; Niepelt, R.; Geburt, S.; Gutsche, C.; Regolin, I.; Prost, W.; Tegude, F.; Stichtenoth, D.; Schwen, D.; Ronning, C. *Small* **2009**, *5* (22), 2576–2580.
- (12) Borschel, C.; Ronning, C. *Nucl. Instrum. Methods Phys. Res., Sect. B* **2011**, *269* (19), 2133–2138.
- (13) Johannes, A.; Noack, S.; Wesch, W.; Glaser, M.; Lugstein, A.; Ronning, C. *Nano Lett.* **2015**, *15* (6), 3800–3807.
- (14) Wutzler, R.; Rebohle, L.; Prucnal, S.; Bregolin, F. L.; Hübner, R.; Voelskow, M.; Helm, M.; Skorupa, W. *J. Appl. Phys.* **2015**, *117* (17), 175307.
- (15) Watt, M.; Sotomayor Torres, C. M.; Arnot, H. E. G.; Beaumont, S. P. *Semicond. Sci. Technol.* **1990**, *5* (4), 285–290.
- (16) Newman, R. C. *Semicond. Sci. Technol.* **1994**, *9* (10), 1749–1762.
- (17) Sutter, E. A.; Sutter, P. W.; Uccelli, E.; Fontcuberta i Morral, A. *Phys. Rev. B: Condens. Matter Mater. Phys.* **2011**, *84* (19), 193303.
- (18) Schmidt, V.; Senz, S.; Gösele, U. *Nano Lett.* **2005**, *5* (5), 931–935.
- (19) Sze, S. M.; Irvin, J. C. *Solid-State Electron.* **1968**, *11* (6), 599–602.
- (20) Ahn, B. H.; Shurtz, R. R.; Trussell, C. W. *J. Appl. Phys.* **1971**, *42* (11), 4512–4513.
- (21) Spicer, W. E.; Liliental-Weber, Z.; Weber, E.; Newman, N.; Kendelewicz, T.; Cao, R.; McCants, C.; Mahowald, P.; Miyano, K.; Lindau, I. *J. Vac. Sci. Technol., B: Microelectron. Process. Phenom.* **1988**, *6* (4), 1245–1251.
- (22) Ketterer, B.; Mikheev, E.; Uccelli, E.; Fontcuberta i Morral, A. *Appl. Phys. Lett.* **2010**, *97* (22), 223103.
- (23) Michaelson, H. B. *IBM J. Res. Dev.* **1978**, *22* (1), 72–80.
- (24) Shichijo, H.; Hess, K. *Phys. Rev. B: Condens. Matter Mater. Phys.* **1981**, *23* (8), 4197–4207.
- (25) Cavassilas, N.; Aniel, F.; Fishman, G.; Adde, R. *Solid-State Electron.* **2002**, *46* (4), 559–566.
- (26) Zanoni, E.; Manfredi, M.; Bigliardi, S.; Paccagnella, A.; Pisoni, P.; Tedesco, C.; Canali, C. *IEEE Trans. Electron Devices* **1992**, *39* (8), 1849–1857.
- (27) Zappe, H. P. *Semicond. Sci. Technol.* **1992**, *7* (3), 391–400.
- (28) Adachi, S. *Handbook on Physical Properties of Semiconductors*; Springer Science & Business Media, 2004; Vol. 2.
- (29) Onodera, K.; Nishimura, K.; Furuta, T. *IEEE Trans. Electron Devices* **1999**, *46* (11), 2170–2177.
- (30) Kittel, C. *Introduction to Solid State Physics*; Wiley & Sons: New York, 2005; pp 106–128.
- (31) Strauch, D.; Dorner, B. *J. Phys.: Condens. Matter* **1990**, *2* (6), 1457.
- (32) Burr, K. C.; Tang, C. L. *Appl. Phys. Lett.* **1999**, *74* (12), 1734–1736.
- (33) Bude, J.; Hess, K. *J. Appl. Phys.* **1992**, *72* (8), 3554–3561.